Chapter 3

Selective detection of organic vapors using TiO_2 nanotubes-based single sensor

3. 1 Introduction

In general, metal oxide-based sensors possess very poor selectivity towards a particular VOC when a similar class of interfering VOCs are present in the ambient [1]. Therefore, different techniques were adopted in the past for improving the selectivity of these types of sensors as discussed in sec. 1.5 of Chapter 1. In an attempt to detect a particular VOC with high selectivity, a new measurement technique is proposed in this chapter. For this, Au/TiO_2 nanotubes/Ti type of sensor was used to detect a range of VOCs and their concentration. This type of sensor exhibited both resistive and capacitive types of vapor sensing as discussed in Chapter 2. This property of the sensor was utilized to develop a new technique in which both resistive and capacitive responses of the sensor were measured upon exposure to target VOC. An algorithm was derived from these two responses which resulted in the formulation of a new constant term "S" (selectivity constant). This term was found to have a distinctive numerical value for different VOCs and independent of the concentration of target VOC. "S" values for different VOCs were calculated and saved as the reference "S" values. To identify the unknown VOC and its concentration, firstly,the "S" value of the unknown VOC was calculated, and then matched with the reference "S" values. The proposed selectivity technique was successfully tested at room temperature for four different VOCs; namely methanol, ethanol, acetone, and 2-propanol.

3. 2 Experimental setup for VOC sensing

TiO_2 nanotubes were grown by electrochemical anodization with a restricted supply of H_2O in electrolyte [2]. The method of synthesis of TiO_2 nanotubes was similar to the

steps discussed in sec. 2.2 (Chapter 2) with only a change in electrolyte composition. In this synthesis, high purity Ti foil (99.99%) was anodized at room temperature using an ethylene glycol-based electrolyte having 5 vol.% of DI water and 0.5 wt.% of NH_4F. The steps involved in fabricating TiO_2 nanotubes-based sensor were also similar to the steps discussed in sec. 2.2 (Chapter 2). For sensor study, the resistance and capacitance values of the sensor were measured simultaneously upon exposure to different VOCs by using an LCR meter. Different VOCs were injected into a sealed chamber by using a micro-syringe as discussed in Chapter 2. The concentration of VOCs (methanol, ethanol, acetone, and 2-propanol) was varied in the range of 100-300 ppm with an interval of 50 ppm. In general, the sensing study was performed at room temperature (27 °C) while maintaining 40% relative humidity (RH). However, to study the effect of RH on the response of the sensor, the following ambient was used i.e. (i) dry synthetic air, (ii) 40% RH, and (iii) 85% of RH in the background upon exposure to 200 ppm of test VOC (methanol). Different relative humidity levels were maintained by using a flow-through arrangement where dry air was injected through a bubbler (saturator) and a mixer and the level of relative humidity level was measured by using a hygrometer.

3. 3 Characterizations of TiO_2 nanotubes

The developed TiO_2 nanotubes were characterized by using different tools like Field Emission Scanning Electron Microscopy (FESEM), X-ray diffraction (XRD, Cu Kα radiation, $\lambda = 1.54$ Å), Transmission Electron Microscopy (TEM), Photoluminescence (PL) spectroscopy and X-ray Photoelectron Spectroscopy (XPS). FESEM images (Fig. 3.1 (a) and (b)) authenticate the formation of highly ordered and porous TiO_2 nanotubes with a high aspect ratio. Inner diameters and lengths of the tubes were measured in the range of 110–150 nm and 2.5-2.7 μm, respectively. This type of structure offers abundant adsorption sites and high surface to volume ratio which enhanced the adsorption possibilities of VOC molecules and thus resistive response of

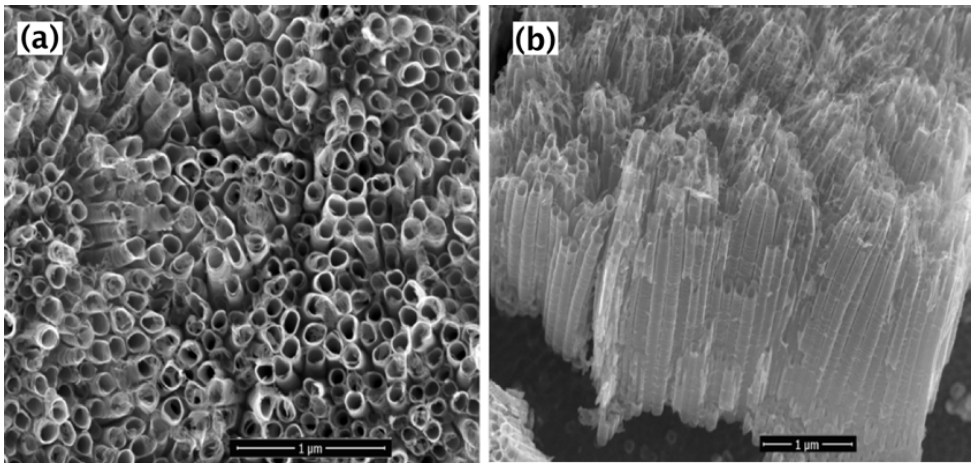

Fig. 3.1 FESEM images of TiO_2 nanotubes/Ti sample showing (a) top view and (b) side view.

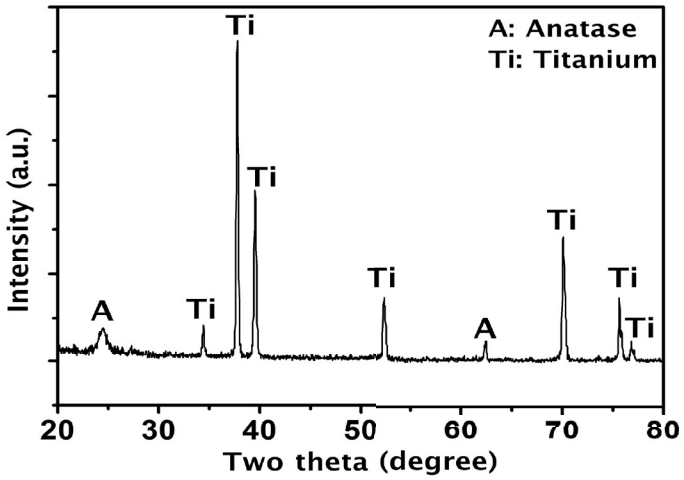

Fig. 3.2 XRD spectra of TiO_2 nanotubes/Ti sample.

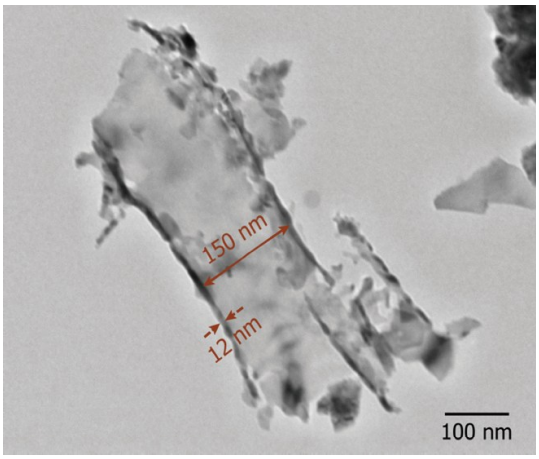

Fig. 3.3 TEM image of TiO_2 nanotubes.

the sensor increases significantly even at low concentration and low temperature [3]. The porous nature of TiO_2 nanotubes is suitable for capacitive sensing also as target VOC can occupy the pores and void regions both. A large area of empty space facilitates a larger diffusion of VOC molecules in this area. This results in a large variation in the magnitude of the dielectric constant of medium and hence capacitance of the sensor changes significantly [4].

XRD spectra of the TiO_2 nanotubes/Ti sample is shown in Fig. 3.2. XRD pattern reveals a high-intensity peak of TiO_2 anatase (101) crystallinity (at $2\theta = 25.3°$) which is authenticated from JCPDS File No. 21-1272. Another low-intensity anatase peak of (213) crystallinity at $2\theta = 62.7°$ was also observed in XRD spectra. Several Ti peaks of metallic titanium (from JCPDS File No. 44-1294) were observed as TiO_2 nanotubes were grown on the Ti substrate. Also, the grown nanotubes were well crystallized into anatase phase and no transition of phase from anatase to rutile was observed. TiO_2 anatase is highly desirable in gas sensing applications as anatase offers higher electron mobility than rutile, leading to faster response and higher sensitivity [5]. The TEM micrograph of TiO_2 nanotubes is depicted in Fig. 3.3 where inner diameter and wall thickness of the tube were measured as 150 nm and 12 nm, respectively. These results are in well agreement with the FESEM observations showing highly oriented and well-structured cylindrical shapes of grown nanotubes.

The PL spectra of TiO_2 nanotubes/Ti sample was measured in a wavelength range of 325-575 nm at 27 °C with 300 nm excitation wavelength. Fig. 3.4 shows the PL spectra of TiO_2 nanotubes/Ti sample where two distinct emission peaks were observed. The emission peaks at 3.21 eV in the UV region and at 2.64 eV in the visible region corresponds to band edge emission and oxygen vacancy related peaks, respectively. Thus, the PL spectra authenticated that oxygen vacancies were present in the grown nanotubes, and hence making TiO_2 highly non-stoichiometric in nature. To get further information about chemical composition/states of nanotubes, TiO_2 nanotubes/Ti sample was characterized by using the XPS technique. Fig. 3.5 (a) shows

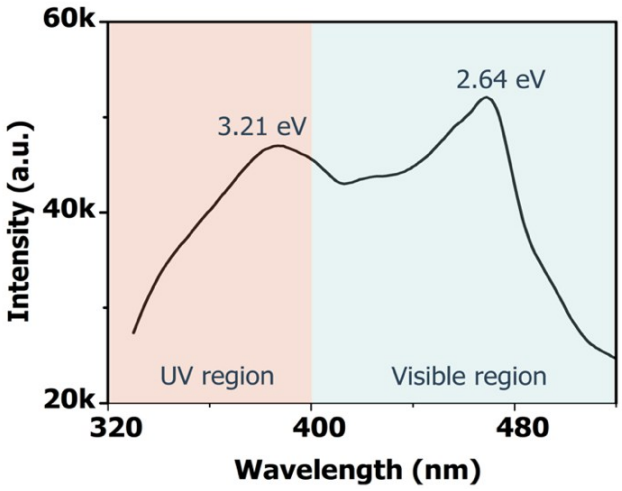

Fig. 3.4 PL spectra of TiO_2 nanotubes/Ti sample.

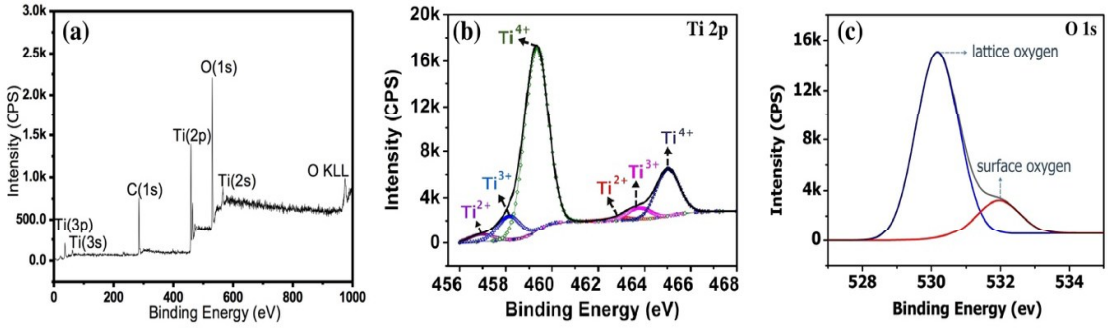

Fig. 3.5 (a) XPS survey spectra of TiO_2 nanotubes/Ti sample; High resolution XPS spectra with fitted peaks of (b) Ti(2p), and (c) O(1s).

Table 3.1 Details of de-convoluted XPS spectra of TiO_2 nanotubes.

TiO_2 state	*Area*	*Position (eV)*
2p $_{1/2}$ (+4)	92833.57	464.989
2p $_{1/2}$ (+3)	2949.036	463.585
2p $_{1/2}$ (+2)	1814.792	462.375
2p $_{3/2}$ (+4)	197261.6	459.265
2p $_{3/2}$ (+3)	6288.154	457.763
2p $_{3/2}$ (+2)	3567.775	456.207

XPS survey scan of TiO_2 nanotubes on Ti substrate. High intensity binding energy peaks of core level (Ti2p, Ti3p, O1s, and C1s) along with the O KLL (where "K" represents energy level of core hole, "L" is the energy level from which K level is filled, "L" is the energy level of Auger electron) auger line are clearly observed. As the escape depth of emitted photo electrons are very much limited within few nanometers only, therefore, XPS spectra represent details of 1-D TiO_2 nanotubes only (not Ti substrate) even they are hollow in shape.

Fig. 3.5 (b) represents the high resolution XPS spectrum of Ti2p BE peaks along with their various deconvolution components. Various possible oxidation states of Ti (+2, +3, +4), originated from the partial O_2 vacancies within the TiO_2 nanotubes are shown here. A quantitative analysis of different peak intensities clearly reveals that the Ti is mostly of Ti^{+4} states, along with a minor percentage of sub-oxidation states. The de-convoluted Ti2p binding energy spectrum is fitted with three titanium doublets representing the oxidation states. The main contribution comes from the Ti^{+4} oxidation state of TiO_2 nanotubes, centered at 464.99 eV ($2p_{1/2}$) and 459.26 eV($2p_{3/2}$). No impression of the metallic Ti^0 state is present in spectra. This finding is somehow contradictory with XRD observation where the diffraction peaks originated from the metallic Ti substrate have clearly been noticed. As the XPS technique is an extremely surface sensitive and the escape depth of the emitted photoelectrons is limited within a few nm only, it is not possible to get any kind of information from the Ti substrate. Whereas, the penetration depth of the X-ray in XRD can extend up to several 100 nm which can easily access the Ti substrate information. However, a minor percentage of TiO (2%) and Ti_2O_3 (3%) formation has clearly been observed. The BE peaks at 463.58 eV ($2p_{1/2}$) and 457.76 eV ($2p_{3/2}$) are attributed to the Ti^{+3} oxidation state of Ti_2O_3, whereas the BE peaks centered at 462.37 eV ($2p_{1/2}$) and 456.21 eV ($2p_{3/2}$) can be correlated to the Ti^{+2} oxidation state of TiO formation. A relative BE shift of about 1.4 eV for each oxidation state starting from Ti^{+2}, Ti^{+3}, Ti^{+4} towards the higher energy has been noticed. Moreover, the ratio of BE peak intensities for $2p_{3/2}$ to $2p_{3/2}$ is found

to be having close proximity to the theoretical value of 2. All these findings confirm the formation of anatase phase of TiO_2. Also, for a better understanding and clarity, every detail of the de-convoluted spectra is summarized in Table 3.1.

Fig. 3.5 (c) shows the XPS spectrum of O1s along with its deconvolution peaks at 530.1 eV and 532 eV. The lower BE peak at 530.1 eV corresponds to the oxygen atom which is chemically bonded within TiO_2 lattice (Ti-O) whereas another higher BE peak at 532 eV corresponds to the oxygen molecule or any hydroxyl group which was physiosorbed on the surface of nanotubes. The lower BE of the chemically bonded O1s can be related to the relative electronic exchange between the Ti and O atoms [6]. Therefore, all XPS results clearly indicate the formation of a reduced titanium dioxide (Ti_nO_{2n-1}, n=1 and 2) nanotubes array which further suggests the existence of positively charged oxygen vacancy type defects (V_C^{2+}) [7].

The sensing property of TiO_2 nanotubes mainly depends on the surface structure and sensing performance can be enhanced in the presence of defects. Oxygen vacancies related defects increase the oxygen adsorption and surface catalytic sites on the surface and hence, makes the sensor more sensitive towards the target VOC [8]. Since, this work is intended to sense VOCs at room temperature, therefore, the surface of TiO_2 nanotubes should have sufficient adsorption sites for efficient vapor sensing.

3. 4 Technique for selective detection of VOCs

VOC sensing properties of the sensor were examined under different concentrations of methanol, ethanol, acetone, and 2-propanol. The sensor showed both resistive and capacitive changes for different VOCs as two electrodes of the sensor was configured vertically to each other. Resistive and capacitive changes of the sensor upon exposure to 100-300 ppm of above mentioned VOCs in a step of 50 ppm were captured for each VOC. Fig. 3.6 (a) shows resistive change of the sensor for different VOCs with complete response and recovery behavior. Fig. 3.6 (c) represents the magnified view of Fig. 3.6 (a) with detailed response behavior and an incomplete recovery. It was found out that

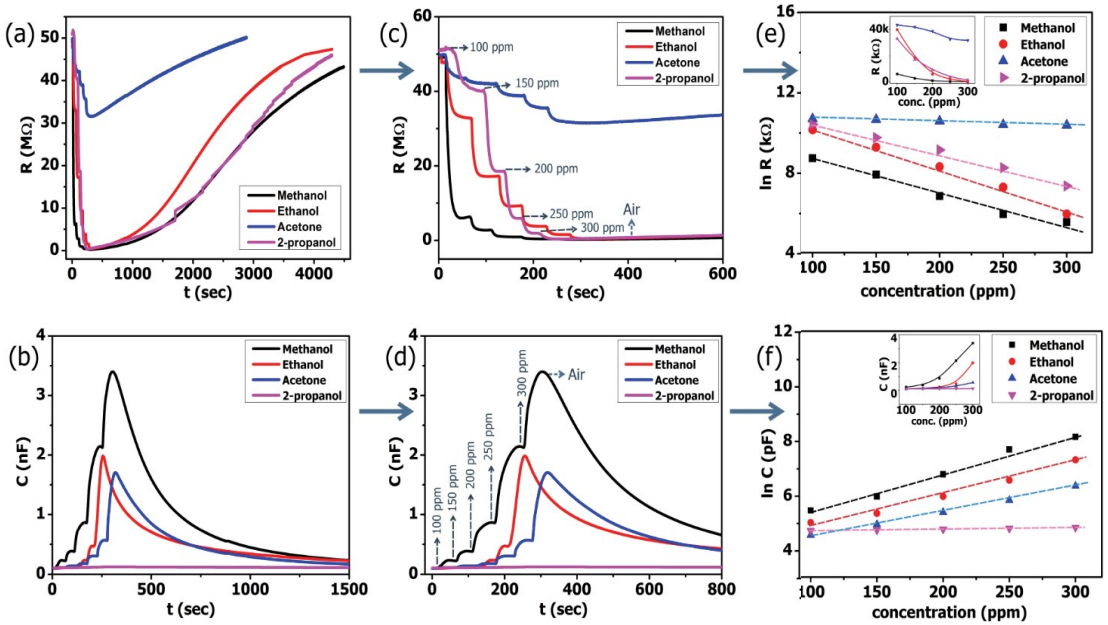

Fig. 3.6 (a) Transient resistive change and, (b) transient capacitive change of the sensor upon exposure to methanol, ethanol, acetone, and 2-propanol; (c) Magnified version of Fig. 3.6 (a) for showing resistive response details and, (d) magnified version of Fig. 3.6 (b) for showing capacitive response details; (e) ln(R) of the sensor vs different VOCs concentration, and (f) ln(C) of the sensor vs different VOCs concentration when concentration of VOCs was increased from 100 ppm to 300 ppm with a step size of 50 ppm.

the sensor showed maximum resistive response towards methanol and sensitivity decreased with the following sequence: ethanol>2-propanol>acetone. In the same way, Fig. 3.6 (b) shows capacitive response of the sensor for different VOCs with complete response and recovery behavior. Fig. 3.6 (d) represents the magnified version of Fig. 3.6 (b) with detailed response behavior and an incomplete recovery. It was found out that the sensor showed maximum capacitive sensitivity towards methanol and sensitivity decreased with the following sequence: ethanol>acetone>2-propanol. Thus, resistance and capacitance of the sensor were decreased and increased, respectively upon exposure to reducing vapor ambient. Also, as to comprehend from Fig. 3.6 (a) and (b), the sensor was able to sense different VOCs both in terms of resistive and capacitive change and hence the problem of selectivity towards a particular VOC remains a key issue.

Table 3.2 Sensor characteristics towards 200 ppm of methanol at different RH levels.

Ambient	*Resistive sensitivity (%)*	*Capacitive sensitivity (%)*	*Resistance baseline (MΩ)*	*Capacitance baseline(pF)*
Dry air	95.8	824	50±4	98±4
40% RH	95.3	805	49±3	98±2
85% RH	90	773	45±3	100 ±2

To examine the humidity effect on TiO_2 nanotubes-based sensor, resistive and capacitive change of the sensor operated at room temperature were measured upon exposure to 200 ppm of methanol with (i.) dry synthetic air, (ii.) 40% RH and (iii.) 85% of RH in the background. Table 3.2 shows resistive and capacitive sensitivity, resistance and capacitance baseline values at different RH levels. The sensor exhibited the maximum resistive response of 95.8% for dry air, remained almost the same as 95.3% for 40% RH and decreased to 90% for 85% RH. Thus, sensitivity of the sensor get reduced with the increase of RH level which was attributed to the dissociation of H_2O molecules into OH^- ions that get adsorbed on the surface of TiO_2 nanotubes. These ions hindered the adsorption of target VOCs, and thus the sensitivity of the sensor gets reduced. The baseline resistance of the sensor was decreased with an increase of RH level due to the formation of Ti-OH dipoles on the surface of nanotubes. This phenomenon produced free electrons, and hence resistance of the sensor device reduced with increase of RH level. Baseline capacitance of the sensor depends upon the polarization and operating frequency. With increase of RH level, polarization of the dielectric medium increases which tends to enhance capacitance value of the sensor. However, capacitance becomes independent of RH level at higher frequency, and thus a negligible change in baseline capacitance and capacitive sensitivity were observed with RH as shown in Table 3.2 [9]. Thus, the performance of the sensor was remained intact at moderate relative humidity level.

From Fig. 3.6 (c), natural logarithm of changed resistance values of the sensor

for 100, 150, 200, 250 and 300 ppm were calculated for methanol, ethanol, acetone, and 2-propanol and plotted in Fig. 3.6 (e). Similarly, Fig. 3.6 (f) shows plotted data of natural logarithmic capacitance change of the sensor for 100, 150, 200, 250 and 300 ppm of methanol, ethanol, acetone, and 2-propanol (using Fig. 3.6 (d)). The inset in Fig. 3.6 (e) and (f) correpond to actual changed resistance and capacitance values of the sensor for different concentrations of VOCs. It was found out that resistance (R in kΩ) and capacitance (C in pF) of the sensor had a natural logarithmic response with vapor concentration (G in ppm) as shown in Fig. 3.6 (c) and (d), respectively and this behavior can be represented by eq. 3.3 and 3.4.

$$\ln (R) = -m_r G + \ln (K_1) \tag{3.1}$$

$$\ln (C) = -m_c G + \ln (K_2) \tag{3.2}$$

where, 'R' and 'C' denote resistance and capacitance of the device in a vapor ambient having concentration level of 'G' ppm. 'K_1' and 'K_2' represent baseline values of resistance and capacitance of the device, respectively. 'm_r' and 'm_c' represent slopes of the straight line of eq. 3.3 and 3.4, respectively. Fig. 3.6 (c) and (d) clearly show that ln(R) and ln(C) of the sensor have a linear relationship with vapor concentration as represented in Fig. 3.6 (e) and 3.6 (f), respectively where different lines correspond to different vapors. Therefore, if, R_1 and C_1 represent resistance and capacitance of the sensor in the exposure of G_1 ppm of any vapor and R_2 and C_2 represent the resistance and capacitance in the exposure of G_2 ppm of the same vapor, then eq. 3.3 can be represented with the help of eq. 3.1 and 3.2 as

$$\frac{\ln(R_2/R_1)}{\ln(C_2/C_1)} = -\frac{m_r}{m_c} \tag{3.3}$$

The magnitude of the ratio of 'm_r' and 'm_c' (in percentage) gives a unique parameter for each VOC and is denoted as 'selectivity constant' (S) as shown in eq. 3.4.

$$S = \left| -\frac{m_r}{m_c} \right| \times 100 \tag{3.4}$$

The values of m_r, m_c, and S were calculated from Fig. 3.6 (e) and (f) for methanol, ethanol, acetone, and 2-propanol and represented in Table 3.3. As evident from Table 3.3, the numerical values of 'S' were found to be unique and concentration independent for each VOC.

Table 3.3 Values of resistive slope, capacitive slope, and selectivity constant for different VOCs.

S. No.	*VOCs*	*Resistive slope (m_r)*	*Capacitive slope (m_c)*	*S (%)*
1	2-propanol	-0.00812	0.000537	1512
2	Methanol	-0.01923	0.01059	181.5
3	Ethanol	-0.01065	0.006851	155.4
4	Acetone	-0.00126	0.003059	41

3. 5 Blind test: Unknown VOC detection

Fig. 3.7 (a) and (b), respectively show resistive and capacitive response of the sensor operating at room temperature for an unknown VOC. To identify the unknown vapor and its concentration, baseline resistance (R_1 =49.3 MΩ) and capacitance (C_1 =92.7 pF) of the sensor were recorded in air ambient. Afterward, the maximum change of resistance (R_2 =0.934 MΩ) and capacitance (C_2 =798.6 pF) values upon exposure to an unknown VOC were measured from Fig. 3.7 (a) and 3.8 (b), respectively.

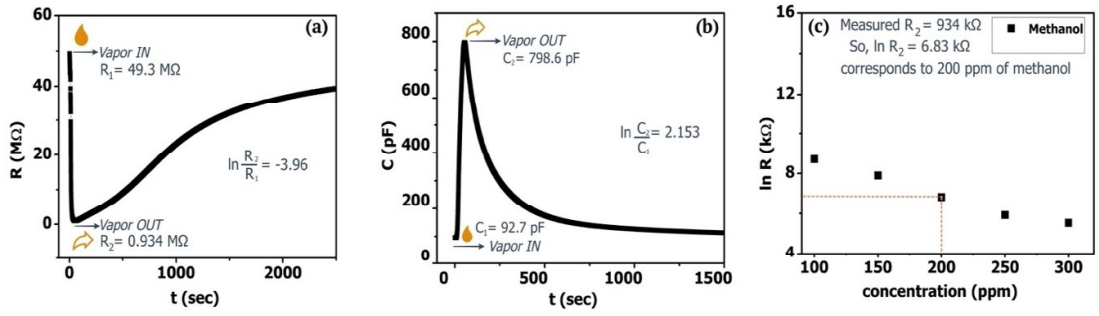

Fig. 3.7 Identification of an unknown VOC; (a) resistive response and (b) capacitive response of the sensor upon exposure to an unknown VOC and concentration. (c) Graphical method to measure the concentration of target VOC after calculating "S" value.

After this, the value of selectivity constant (S) was calculated as 183 by using eq. 3.3 and 3.4. This value was found to be very similar to the pre-calculated 'S' value of methanol (181.5) as shown in Table 3.2. So, the unknown vapor was identified as 'methanol'. After successful identification of the unknown vapor, concentration (G) of the detected vapor can be calculated either analytically or graphically. Analytically, G can be calculated by using either eq. 3.1 or eq. 3.2. Graphically, G can be calculated from ln(R) vs G graph for methanol (Fig. 3.6 (c)) where the measured value of $\ln(R_2)$ corresponds to 200 ppm of methanol as shown in Fig. 3.7 (c).

3. 6 Sensing mechanism of TiO_2 nanotubes-based sensor

A brief overview of the sensing mechanism of the sensor was already discussed in sec. 2.5.3 (Chapter 2). However, this section explains the sensing mechanism of the sensor operating at room temperature and taking into account various chemical reactions which change the conductivity of the sensor. The grown nanotubes were non-stoichiometric in nature having a large number of oxygen vacancies as evident from PL spectra (Fig. 3.4). XPS spectra in Fig. 3.5 (c) also confirmed the availability of surface oxygen in TiO_2 nanotubes at room temperature. The sensitivity of metal oxide based sensors principally depends on the number of available adsorption sites and adsorbed oxygen species (like O_2^-, O^- and O^{2-}) [10]. Also, at room temperature, adsorbed O^- ions dominantly react with VOC molecules. Oxygen vacancies act as "active sites" for the dissociative physical adsorption of oxygen molecules on the surface of TiO_2. An increase of oxygen vacancies resulted in more adsorption of oxygen molecules which enhances the interaction sites for reducing VOCs and this eventually increases the response of the sensor. The resistive response of TiO_2 nanotubes-based sensor can be illustrated with the help of Wolkenstein adsorption-desorption theory [11]. At low/room temperature, oxygen molecules from air ambient get physisorbed on the surface of TiO_2 nanotubes and eventually converted to $O_{2(ads)}^-$ and $O_{(ads)}^-$ ions by taking free electrons from the surface of nanotubes as shown in eq. 3.7 - 3.9.

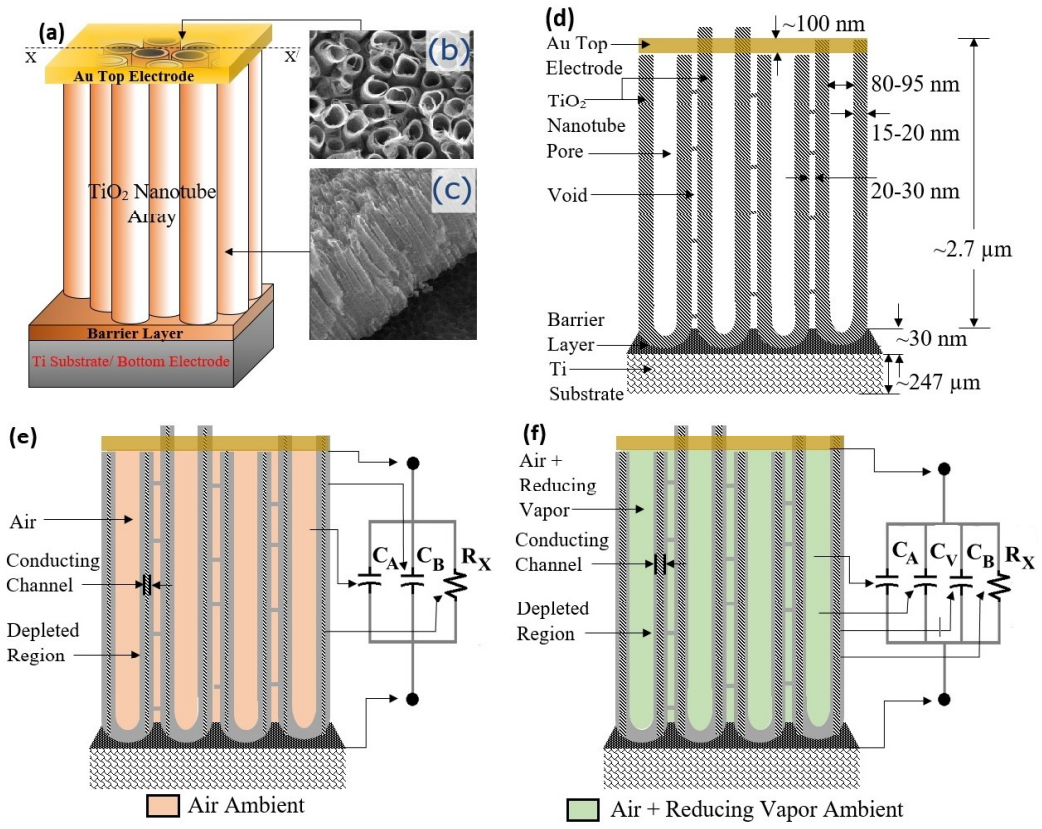

Fig. 3.8 (a) A schematic of 'Au/TiO_2 nanotubes/Ti' sandwich-structured sensor; FESEM images of TiO_2 nanotubes: (b) top view, and (c) side view; (d) Cross-sectional view of the sensor (at XX/ line) with structural dimensions; Device cross-section and R-C circuit model (e) in air ambient, and (f) in reducing vapour ambient.

$$O_{2(gas)} \rightarrow O_{2(ads)} \tag{3.7}$$

$$O_{2(ads)} + e^- \rightarrow O_2^-{}_{(ads).} \tag{3.8}$$

$$O_2^-{}_{(ads)} + e^- \rightarrow 2O^-{}_{(ads)} \tag{3.9}$$

As electrons from the surface of nanotubes get consumed; thus, a depletion region gets formed on the wall of nanotubes which increases the resistance of the sensor in air ambient. Upon exposure to any reducing VOCs, the adsorbed oxygen ions react with VOC molecules which results in the release of electrons. This results in the decrement in resistance of the sensor as the number of free charge carriers get increases. Possible oxidation steps of reducing VOCs (methanol for reference) on the surface of nanotubes at room temperature (27 °C) can be described by eq. (3.10) - (3.19) [12], [8], [9].

$CH_3\text{-}OH_{(gas)} \rightarrow CH_3\text{-}OH_{(ads)}$ (3.10)

$CH_3\text{-}OH_{(ads)} \rightarrow CH_3\text{-}O_{(ads)} + H_{(ads)}$ (3.11)

$CH_3\text{-}O_{(ads)} \rightarrow CH_2\text{-}O_{(ads)} + H_{(ads)}$ (3.12)

$H_{(ads)} + H_{(ads)} \rightarrow 2H^+_{(ads)} + 2e^-$ (3.13)

$2H^+_{(ads)} + 2O^-_{(ads)} \rightarrow 2OH_{(ads)}$ (3.14)

$2OH_{(ads)} \rightarrow H_2O_{(ads)} + O_{(ads)}$ (3.15)

$O_{(ads)} + e^- \rightarrow O^-_{(ads)}$ (3.16)

$CH_3\text{-}OH_{(ads)} + 4O^-_{(ads)} \rightarrow CO_2 + 2H_2O + 4e^-$ (3.17)

$2CH_3\text{-}O_{(ads)} + 4O^-_{(ads)} \rightarrow CO + CO_2 + 3H_2O + 4e^-$ (3.18)

$CH_2\text{-}O_{(ads)} + 4O^-_{(ads)} \rightarrow CO + CO_2 + 2H_2 + 4e^-$ (3.19)

A schematic of the sandwich-structured (Au/TiO_2 nanotubes/Ti) sensor device is shown in Fig. 3.8 (a) which is similar to the schematic discussed in Fig. 2.3. Top and side views of TiO_2 nanotubes as observed by FESEM are shown in Fig. 3.8 (b) and (c), respectively. A cross-sectional view of Au/TiO_2 nanotubes/Ti device at XX$^/$ line (Fig. 3.8 (a)) is represented in Fig. 3.8 (d). Dimensions of nanotubes were measured from the FESEM study and shown in Fig. 3.8 (d). Fig. 3.8 (e) shows cross-sectional schematic of the sensor with the estimated circuit model in air ambient which is similar to the model discussed in sec. 2.4 (Chapter 2). The R-C circuit model which is considered between two electrodes (Au and Ti) in air ambient consists of two capacitive components (C_A and C_B) and one resistive component (R_X). C_A and C_B are the capacitances having free space and TiO_2 nanotubes as dielectric medium, respectively. R_{TiO2} is the resistance of the conducting channel of TiO_2 nanotubes. Due to the adsorption of different oxygen species in air ambient, a depleted region is formed near the surface of n-TiO_2 nanotubes and a thin conducting channel is formed inside the bulk of nanotubes as shown in Fig. 3.8 (e). Thus, in air ambient, the resistance of nanotubes (R_X) is found to be high because of a very thin conducting channel. In reducing vapor ambient, adsorbed oxygen species get removed partially from the surface of TiO_2 nanotubes which lowers the width of depletion region as shown in Fig.

3.8 (f). So, R_X gets reduced in reducing ambient because of the thicker conducting channel. On the other hand, net capacitance (C_X) in-between two electrodes is estimated as C_A+C_B in air ambient (Fig. 3.8 (e)). Due to the introduction of reducing vapors, void regions of nanotubes get filled with vapors resulting in the increased dielectric constant of the medium which has been modeled by adding an extra capacitive component (C_V) in the circuit (Fig. 3.8 (f)). So, the net capacitance of the device is increased in reducing vapor ambient ($C_X = C_A+C_V+C_B$). Therefore, the proposed circuit model shows that effective resistance and capacitance of the device tend to decrease and increase, respectively in reducing vapor ambient.

Room temperature sensing using TiO_2 nanotubes can be explained using the following points:

i. As compared to TiO_2 thin film and other nanostructures, where only the outer surface is responsible for adsorption-desorption of VOCs, TiO_2 nanotubes offer both inner and outer surface for adsorption-desorption which increases the response magnitude of the sensor.

ii. TiO_2 nanotubes were in anatase phase which is reported to be more sensitive towards reducing gases as compared to rutile phase of TiO_2 [13]. Also, the activation energy of TiO_2 in anatase phase (0.19-0.41 eV) is relatively less than rutile phase (0.8 eV) and hence requires less operating temperature [14].

iii. In general, for planer placement of electrodes, high operating temperature is needed because electron has to cross a lot of intergranular potential barrier that exists in-between two nanotubes and thus increases the activation energy. However, in present work, two electrodes were placed vertically in between TiO_2 nanotubes where electrons do not need to cross the intergranular potential barrier. Thus, it facilitates barrier less 1-D electron transport through nanotubes which reduces the operating temperature [2].

Resistive response magnitude (RRM) of the TiO_2 nanotubes based sensor is considered to depend upon multiple parameters like temperature (T), the concentration of target

VOC molecules (N_{VOC}) and free charge carriers (e^-) upon exposure to VOC (N_e), number of oxygen ions per unit area (N_O), reaction rate constant (K) and surface area of TiO_2 nanotubes (Ø) which can be related by using eq. 3.20 and 3.21 [15].

$$RRM = f\left(\frac{K\emptyset N_O N_{VOC}}{N_e}\right) \tag{3.20}$$

$$K = A\exp\left(-\frac{E_a}{k_B T}\right) \tag{3.21}$$

where, A is a time constant and E_a denotes the activation energy. Room temperature provides low but finite energy that may be sufficient for gas sensing if other parameters play a significant role. Usually, both reaction rate constant and concentration of free charge carriers get increased with temperature and therefore sensor achieved the maximum response value at an optimum value of temperature. Also, as evident from eq. (3.20), response of the sensor can be increased by increasing adsorbed oxygen ions and surface area of nanotubes. Since grown TiO_2 nanotubes had large oxygen vacancies and high surface to volume ratio and VOC sensing was achieved even at low/room temperature.

3. 7 Conclusions

Au/TiO_2 nanotubes/Ti type of sandwich-structured device was fabricated for selective identification of various VOCs at room temperature (27 °C). The issue of cross-sensitivity was resolved by developing a technique involving the measurement of both resistive and capacitive change of the sensor upon exposure to different VOCs. Resistance and capacitance of the sensor operating at room temperature had a natural logarithmic response with VOC concentration. This behavior of the sensor was used to derive a new parameter named as selectivity constant ("S") for different VOCs e.g. methanol, ethanol, acetone, and 2-propanol. The numerical value of selectivity constant was found to be unique and concentration independent for a particular VOC and hence, it can be used as a VOC discriminator parameter. Thus, by using the proposed technique, TiO_2 nanotubes based single sensor operating at room temperature

can be used efficiently to identify and quantify different types of VOCs.

References

1. Y. Liu, L. Wang, H. Wang, M. Xiong, T. Yang, G.S. Zakharova, Highly sensitive and selective ammonia gas sensors based on PbS quantum dots/TiO_2 nanotube arrays at room temperature, Sensors and Actuators B 236 (2016) 529-536.
2. A. Hazra, B. Bhowmik, K. Dutta, P.P. Chattopadhyay, P. Bhattacharyya, Stoichiometry, length, and wall thickness optimization of TiO_2 nanotube array for efficient alcohol sensing, ACS Appl. Mater. Interfaces 7 (2015) 9336-9348.
3. A. Hazra, P. Bhattacharyya, Tailoring of the gas sensing performance of TiO_2 nanotubes by 1-D vertical electron transport technique, IEEE Trans. Electron Devices 61 (2014) 3483-3489.
4. K. Dutta, A. Hazra, P. Bhattacharyya, Ti/TiO_2 nanotube array/Ti capacitive device for non-polar aromatic hydrocarbon detection, IEEE Trans. Device and Materials Reliability 16 (2016) 235-242.
5. T. Luttrell, S. Halpegamage, J. Tao, A. Kramer, E. Sutter, M. Batzill, Why is anatase a better photocatalyst than rutile? - Model studies on epitaxial TiO_2 films, Scientific Reports 4 (2015) 1-8.
6. J. Wang, J. Yang, N. Han, X. Zhou, S. Gong, J. Yang, P. Hu, Y. Chen, Highly sensitive and selective ethanol and acetone gas sensors based on modified ZnO nanomaterials, Materials and Design 121 (2017) 69-76.
7. X. Chang, X. Wu, Y. Guo, Y. Zhao, J. Zheng, X. Li, $SnSO_4$ modified ZnO nanostructure for highly sensitive and selective formaldehyde Detection, Sensors Actuators and B 255 (2018) 1153-1159.
8. A. Hazra, K. Dutta, B. Bhowmik, P.P. Chattopadhyay, P. Bhattacharyya, Room temperature alcohol sensing by oxygen vacancy controlled TiO_2 nanotube array, Applied Physics Letters 105 (2014) 081604.
9. B. Bhowmik, P. Bhattacharyya, Highly stable low temperature alcohol sensor based on hydrothermally grown tetragonal titania nanorods, RSC Adv. 5 (2015) 82159-82168.
10. J. Nowotny, T. Bak, L.R. Sheppard, M.K. Nowotny, Reactivity of titanium dioxide with

oxygen at room temperature and the related charge transfer, J. Am. Chem. Soc. 130 (2008) 9984-9993.

11. Y. Qin, Z. Cui, T. Zhang, D. Liu, Polypyrrole shell (nanoparticles)-functionalized silicon nanowires array with enhanced NH_3-sensing response, Sensors and Actuators B 258 (2018) 246-254.
12. A. Hazra, B. Bhowmik, K. Dutta, P.P. Chattopadhyay, P. Bhattacharyya, Stoichiometry, length, and wall thickness optimization of TiO_2 nanotube array for efficient alcohol sensing, ACS Appl. Mater. Interfaces. 7 (2015) 9336-9348.
13. F. Şennik, Z. Çolak, N. Kilinç, Z.Z. Öztürk, Synthesis of highly-ordered TiO_2 nanotubes for a hydrogen sensor, Int. J. Hydrogen Energy. 35 (2010) 4420-4427.
14. E. Sennik, N. Kilinc, Z. Ziya, Electrical and VOC sensing properties of anatase and rutile TiO_2 nanotubes, Journal of Alloys and Compounds 616 (2014) 89-96.
15. N. Hongsith, E. Wongrat, T. Kerdcharoen, S. Choopun, Sensor response formula for sensor based on ZnO nanostructures, Sensors Actuators, B Chem. 144 (2010) 67-72.